

# Non-Iterative SLAM: A Fast Dense Method for Inertial-Visual SLAM

Chen Wang, Junsong Yuan and Lihua Xie\*

**Abstract**—The goal of this paper is to create a new framework of Visual SLAM that is light enough for Micro Unmanned Aerial Vehicle (MUAV) based on inertial sensor and depth camera. Feature-based and direct methods are two mainstreams in Visual SLAM. Both methods minimize photometric or reprojection error by iterative solutions, which are always computationally expensive. To overcome this problem, we propose a non-iterative approach to match point clouds directly. In particular, a new inertial-visual framework is proposed to reduce computational requirement in two steps. First, the attitude and heading reference system (AHRS) and axonometric projection are utilized to decouple the 6 Degree-of-Freedom (DoF) data, so that point clouds can be matched in independent spaces respectively. Second, the matching process is carried out in frequency domain by Fourier transformation, which reduces computational requirements dramatically and provides a closed-form non-iterative solution. In this manner, the time complexity can be reduced to  $\mathcal{O}(n \log n)$  where  $n$  is the number of matched points in each frame.

To the best of our knowledge, this method is the first non-iterative approach for data association in Visual SLAM. Compared with the state of the arts, it runs at faster speed and obtains 3D maps with higher resolution yet still with comparable accuracy.

## I. INTRODUCTION

Self-localization-mapping is one of the most basic capabilities of autonomous robots, which has received increasing attention in tandem with the development of hardwares, such as smarter sensors and faster processors [1]. However, 3D SLAM algorithms are difficult to be applied directly to Micro Unmanned Aerial Vehicle (MUAV) systems due to the following reasons. First, different from ground robots, MUAVs are unable to provide odometer information to correct unacceptable drift in pure vision and GPS-denied SLAM systems. Second, MUAVs can only provide limited computation resources, such as embedded systems with ARM processors, due to payload and power limitations. Third, dense map, which is crucial for higher level applications, such as object detection and scene understanding, requires more computational resources to produce [2]. Therefore, the motivation of this paper is to develop a light visual SLAM system that can be carried by MUAVs and achieve faster computational speed and denser maps with sufficient accuracy for navigation and control purposes.

Despite the progresses, one limitation of the existing Visual SLAM methods is that the time complexity of visual data association is too high for limited computational

\*Corresponding Author.

The authors are with the School of Electrical and Electronic Engineering, Nanyang Technological University, 50 Nanyang Avenue, 639798, Singapore email: wang.chen@zoho.com; jsyuan@ntu.edu.sg; elhxie@ntu.edu.sg

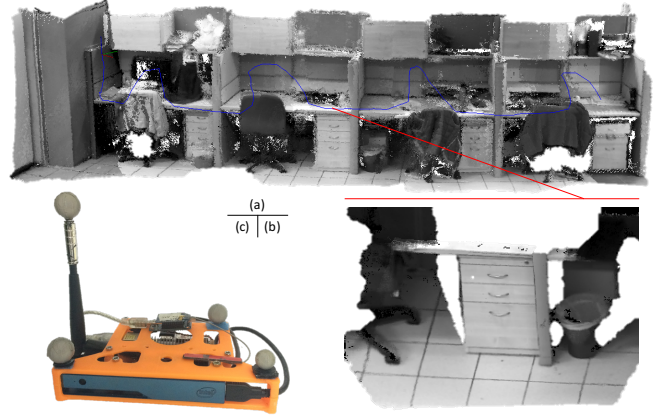


Fig. 1. A work place map (a) with resolution 0.005m is created by Non-Iterative SLAM (NI-SLAM) in real-time on an ultra-low power CPU with Scenario Design Power (SDP) of 2W shown in Table I. The map is shown without post-processing. (b) is an example of refined axonometric image. (c) is the integrated ultra-low power hardware platform, including an inertial sensor myAHRS+, Intel RealSense Robotic Development kit and a ZigBee module for receiving groundtruth from a motion capture system.

resources of MUAV, especially when the dense maps are required. In the SLAM problem, visual data association tries to relate the sensors' measurements with the landmarks inside the maps [3]. It can be categorized as feature-based and direct methods.

Feature-based methods require a time consuming processing loop, including feature detection, extraction, matching, outliers rejection and motion estimation. Generally, more than one thousand features are required to be extracted in only one image [3]. Features like SIFT [4] are robust but computationally intensive, while features like SURF [5] and ORB [6] are faster but less robust. To remove feature matching outliers, iterative methods like RANSAC [7] which are very time consuming, are often used. Moreover, to fit a good motion model, other iterative methods (e.g. Gauss-Newton) are needed to minimize the reprojection error [2], [8], [9]. Therefore, the feature extraction process and iterative solutions like RANSAC and Gauss-Newton are the main computational burden for feature-based methods.

For direct methods, iterative solutions also play an important role and have become the bottleneck. Iterative Closest Point (ICP) is a class of algorithms that is often used when 3D point clouds need to be matched. Its time complexity is given by  $\mathcal{O}(n^2)$  [10] which is very high to be carried out online ( $n$  is the number of points to be matched). Alternatively, motion model can be estimated by the minimization of photometric error over all pixels [9], [11]–[15]. Although

feature extraction is not needed any more, it still needs heavy computation, since all the image points are involved in the minimization process based on iterative methods such as Gauss-Newton method.

To reduce the computational burden, we argue that the iterative solutions of data association should be replaced by a closed-form solution, which means a new objective function may be needed. Interestingly, we find that if the 6 Degree-of-Freedom data (3D point clouds) can be decoupled into sub-spaces with lower DoF, the data association problem can be formulated as a classic regression problem with quadratic objective function, where a closed-form solution becomes feasible to be carried out online. Recent works also proposed to fuse information from Inertial Measurement Unit (IMU) to improve performance. However, since existing approaches still require iterative solution, the information provided by IMU is not able to significantly reduce the computation complexity of visual data association. To fully utilize the inertial information and reduce the complexity, we propose to decouple the 6 DoF data by attitude and heading reference system (AHRS) and axonometric projection. The key difference between IMU and AHRS is that AHRS is equipped with an on-board processing unit that is able to provide superior reliable and accurate attitude and heading information versus an IMU which just delivers sensor data to an additional device. In summary, the main contributions of this paper are:

- We propose a novel Inertial-Visual SLAM framework, which leverages on AHRS and any 3D sensors that can provide 3D point clouds (e.g. RGB-D/stereo camera and 3D laser scanner). It is light enough to be carried out by low-power on-board processors of MUAV and is able to produce very high resolution maps.
- To enable faster data association, we propose a regression-based formulation and find a non-iterative solution with complexity  $\mathcal{O}(n \log(n))$  by leveraging Fourier Transform, where  $n$  is the number of points. First, the 6 DoF point clouds are decoupled into 3 rotational DoF and 3 independent 1D translational DoF. Second, instead of fitting a motion model iteratively, we estimate the camera motion by training the decoupled data online with a fast closed-form solution.
- A fast dense map refinement/fusion method is proposed based on a moving average. The missing information in one key point cloud can be complemented by other point clouds with only the complexity  $\mathcal{O}(n)$ .

## II. RELATED WORK

It is worth mentioning the parallel work of SLAM, Visual Odometry (VO). More specifically, VO only requires the incremental estimation of the 6 DoF pose transformation, whereas SLAM needs to map surrounding environments and recognizes the spot when robot revisits that location [16]. Since VO can be part of SLAM, we will no longer distinguish them unless necessary, and this paper focuses on the estimation of incremental poses and the 3D map generation without loop closure detection. This section will

review recent works both on visual data association and fusion with inertial sensors.

### A. Data Association

The idea of feature-based method is that the incremental pose transformation can be estimated by well matched features. During the feature-detection step, salient key features that are likely to be matched well in other images are selected. Basically, there are two main approaches to find the corresponding features [16]. One is to extract features using local search techniques [9] and match them between the latest image and key-frame [17]. This method is suitable for images taken from nearby viewpoints. The other one is to extract features independently and match them in a sequence of images based on similarity descriptors [18]. This is more suitable for large motion between two viewpoints. Some features descriptors for 3D point clouds [19] have received increasing attentions. More feature extracting methods for 2D images, such as FAST [20], SIFT [4], SURF [5] and ORB [6] have been widely used in both monocular [17] and RGB-D [2] SLAM. The matched features will be refined to remove outliers by the RANSAC algorithm, and the iterative gradient method such as Gauss-Newton will be utilized to find a motion transformation. Only information that conforms to the feature type can be used in feature-based method, which causes substantial loss of structural information.

In contrast with feature-based methods, direct methods match all image points directly, resulting in a denser map which provides substantially more information about the geometry of environment. Based on the minimization of photometric error, direct methods have been developed for monocular [13], stereo [21] and RGB-D [11] cameras. Since there is no descriptor, only local search techniques can be used to find the corresponding pixels, hence this is not suitable for large motion between two viewpoints. Combining with feature correspondences [9] or depth filter [22], the monocular direct SLAM methods are able to achieve good performance. Again, since all the image points are involved to fit a pose transformation model by an iterative solution, the time complexity is too high for an MUAV system. Furthermore, compared with monocular camera, RGB-D camera or 3D laser scanner produces more information which is more challenging for direct methods to process.

### B. Inertial Fusion

Inertial sensors provide an additional constraint for the pose transformation estimation which can help to speed up the pure Visual SLAM system [23]. Loosely-coupled methods [15] fuse the pose estimation from SLAM and IMU independently. While tightly-coupled methods which estimate the states jointly give a better performance in terms of accuracy, but have an additional complexity due to the involvement of a non-linear optimization process [24], [25]. In recent years, IMU fusion has been proposed for feature-based-monocular [26], feature-based-stereo [24], direct-stereo [15], [27] and direct-monocular [23] systems.

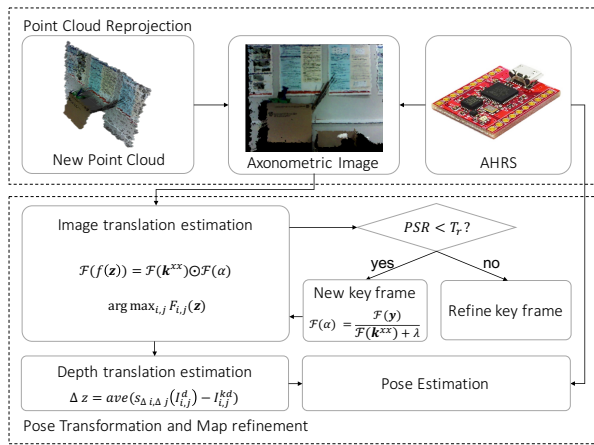


Fig. 2. The proposed inertial-visual framework. Only when the maximum response value is lower than a threshold, a new key point cloud is inserted and the combination weights  $\alpha_i$  are then updated.

### III. ITERATIVE SLAM

The Iterative SLAM minimizes the reprojection or photometric error to estimate the pose transformation. Assume that the camera model  $\pi(\cdot)$  projects 3D point  $p_i$  to image point  $u_i$ , so that  $u_i = \pi(E_{CW}p_i)$  where  $E_{CW}$  is the transform matrix from the world to camera frame. Incremental poses  $E'_{CW}$  are expressed by left-multiplication a vector  $\mu$  with 6 DoF based on exponential mapping, i.e.,  $E'_{CW} = \exp(\mu)E_{CW}$ .

In feature-based methods, feature points  $u_i$  in one image are reprojected to another image  $u'_i$ , so that pose transformation can be estimated by minimizing the reprojection error.

$$\mu^* = \arg \min_{\mu} \sum_i \rho(u'_i - \pi(E'_{CW}\pi^{-1}(u_i, E_{CW}))) \quad (1)$$

where  $\rho$  is a general objective function. In [8], where the FAST corner detector is applied,  $\rho$  is the Tukey biweight function; whereas in [2], [9],  $\rho$  is the  $L_2$ -norm function. For monocular camera, an initial process to obtain the depths of points is needed [8], [9], [17], while for stereo/RGB-D camera, this process can be skipped [28], [29].

In direct methods, new images are aligned with several key frames  $I_r$  by minimizing the photometric error given in (2). Similar expressions can be found in [9], [13]–[15].

$$\mu^* = \arg \min_{\mu} \sum_{i,r} \rho(I_r(u'_i) - I(\pi(E'_{C_r W}\pi^{-1}(u_i, E_{CW})))) \quad (2)$$

where  $\rho(\cdot)$  has the same meaning with (1). Being non-robustness to illumination changes is one of the potential problems of matching pixel intensities [14]. Since (1) and (2) are highly non-linear, the iterative solutions (e.g. Gauss-Newton) are needed. Unfortunately, they are sensitive to initialization and cannot guarantee the global optimal solution.

### IV. NON-ITERATIVE SLAM

To avoid iterative solutions and reduce computational burden, we propose a novel inertial-visual framework shown in Fig. 2. First, in Section IV-A, the 6 DoF point cloud is decoupled and reprojected to axonometric images with

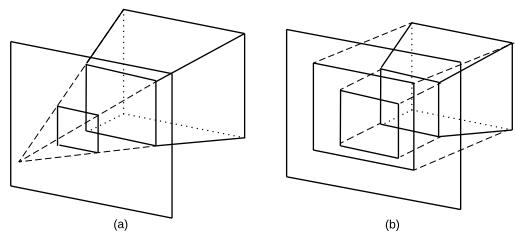


Fig. 3. Differences between perspective and axonometric projections. A quadrangular frustum pyramid can be a rectangle in perspective image (a) when the vertex coincides with the principle point. While for axonometric image (b), the size ratio of the two rectangles will not change. This property will be used in the following association procedure.

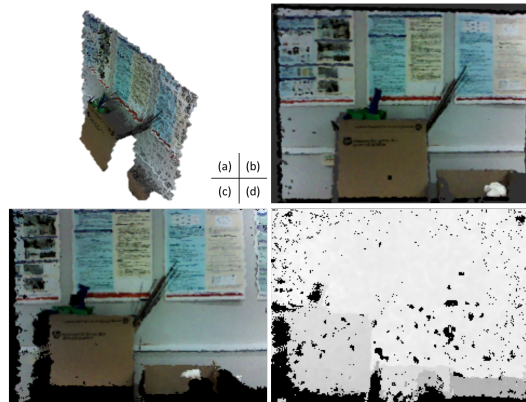


Fig. 4. A point cloud (a) captured by Intel RealSense is rectified by AHRS shown in (b) which is a perspective image. Then it is reprojected to an axonometric color image (c) and axonometric depth image (d). Some black holes can be seen in (c) and (d), since some invisible points in (b) are also projected to the axonometric image plane.

only 1 DoF. Section IV-B demonstrates that the 1 DoF data can be matched by a closed-form non-iterative solution. The decoupled translations are estimated in Section IV-C and IV-D respectively. Finally, refinements of the key point clouds are presented in Section IV-E. It should be noted that the term ‘non-iterative’ is only used for data association, while the mapping and localization of SLAM are still iterative.

#### A. Point Clouds Reprojection

1) *6 DoF to 3 DoF*: A point cloud is a set of data points with 6 DoF  $\mu(x, y, z, \alpha, \beta, \phi)$  in a three-dimensional coordinate system. Normally, points are defined by  $X$ ,  $Y$ , and  $Z$  coordinates with specified color  $R$ ,  $G$ ,  $B$ , and are intended to represent an external surface of an object or an environment (no color information for 3D laser scanner).

To decouple the rotational and translational DoF, we utilize the attitude information from AHRS directly. An AHRS consists of sensors on three axes that provide attitude information for aircraft, including roll, pitch and yaw [30]. The estimated attitude error of an AHRS is only about 1 degree [31], but a pure visual SLAM system has an estimated error of several degrees [32]. In this sense, the 6 DoF data  $\mu(x, y, z, \alpha, \beta, \phi)$  can be reduced to three DoF  $\mu(x, y, z)$  easily.

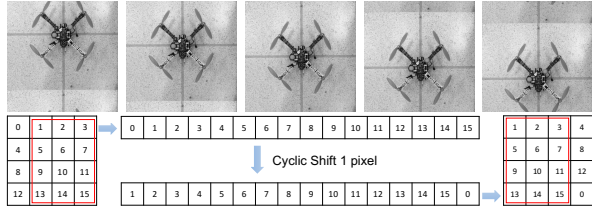


Fig. 5. The axonometric images are expanded into a 1D vector, and cyclic shift of the 1D vector can be mapped to a unique 2D translation in the original image. Since it is one to one mapping, the translation estimation in the 2D image plane can be replaced by a 1D vector. The disadvantage of cyclic shift is the ignored border effect, where the pixels on one side of the original image may be relocated at other side of the new image. However, we will show that cyclic shifts have amazing properties that are able to speed up the matching procedure dramatically.

2) *3 DoF to 2 DoF*: The basic idea for decoupling the 3 translational DoF  $\mu(x, y, z)$  is that the geometry properties in the 3 separate axes must be kept. Therefore, we propose to apply axonometric projection on the rectified point clouds to get axonometric color and depth images.

Different from the perspective projection which projects 3D points on the principle point, the axonometric projection projects points on the axonometric plane shown in Fig. 3. Since the distance ratio between any pair of image points will not change in the axonometric plane, the 3D translation can be estimated in the 2D axonometric image plane followed by 1D translation estimation in the depth direction.

Since the point clouds are generated by pinhole cameras, when they are reprojected on axonometric plane, some black holes may appear. The reason is that some invisible points for pinhole cameras are also projected on the axonometric images. It will be shown that these black holes do not affect the translation estimation and will be filled by the refinement process for the key point clouds in Section IV-E. Fig. 4 shows the procedure that a 6 DoF point cloud is rectified by AHRS then reprojected to axonometric images.

3) *2 DoF to 1 DoF*: The core idea is that the translation of a 2D axonometric image can be treated as 1D translation of an expanded vector, which is illustrated in Fig. 5.

The data decoupling procedure from 6 DoF to 1 DoF does not lose any structural information, since the original 6 DoF data can be restored without additional information.

## B. Translation Pattern Training

The fundamental idea is that we want to learn the pattern of an expanded key axonometric image, so that the translation of a new image can be predicted directly based on the assumption that there is enough overlap between the key and the new frames. Assume that the  $N$  by  $M$  key axonometric image is denoted by a 1D column vector  $\mathbf{x} \in \mathbb{R}^n$ , ( $n = N \times M$ ). Hence the training samples can be defined as  $X = [\mathbf{x}_0, \mathbf{x}_1, \dots, \mathbf{x}_{n-1}]^T$  where  $\mathbf{x}_i$  is obtained from cyclic shifted  $\mathbf{x}$  by  $i$  pixels. Actually,  $X$  is a circulant matrix [33] and can be defined as  $X = C(\mathbf{x})$ , since it can be generated by its first row  $\mathbf{x}^T$ . The training problem is to find a regression function (3) where each sample  $\mathbf{x}_i$  has its own target  $y_i$ , so that when a test sample  $\mathbf{z}$  is given,  $f(\mathbf{z})$

will be corresponding to its translation-related target.

$$y_i = f(\mathbf{x}_i) \quad (3)$$

where  $y_i$  can be any pre-defined real value. Intuitively, if  $y_i = i$ , the translation of the test samples can be predicted directly. However, since only the zero-shift sample  $x_0$  is concerned, in the following tests, the label  $y_0$  is set as 1, while all the others are 0. In this sense, all the non-zero-shift samples are considered as negative samples, which makes the regression function more distinctive.

1) *Linear Case*: The linear regression function is defined as  $f(\mathbf{x}) = \mathbf{w}^T \mathbf{x}$ ,  $\mathbf{w} \in \mathbb{R}^n$ . Given the training samples  $X$ , we can find the coefficient vector  $\mathbf{w}$  by minimizing the squared error over the samples  $\mathbf{x}_i$  and the regression target  $y_i$ .

$$\mathbf{w}^* = \arg \min_{\mathbf{w}} \sum_{i=1}^n (f(\mathbf{x}_i) - y_i)^2 + \lambda \|\mathbf{w}\|^2 \quad (4)$$

where  $\lambda$  is a regularization parameter to prevent overfitting. This is a ridge regression problem and can be solved by setting its first derivative to zero. By defining  $\mathbf{y} = [y_0, y_1, \dots, y_{n-1}]^T$ , (4) has a closed-form solution [34] in complex domain:

$$\mathbf{w}^* = (X^H X + \lambda I)^{-1} X^H \mathbf{y} \quad (5)$$

where  $H$  denotes the conjugate transpose.

For a  $480 \times 360$  axonometric image, where  $n = 172800$ , the inversion of a  $172800 \times 172800$  matrix ( $X^T X + \lambda I$ ) needs to be computed which is impossible to be carried out in real time. However, the interesting thing is that, different from a traditional machine learning problem,  $X = C(\mathbf{x})$  is a circulant matrix. This amazing property makes the solution (5) easy to be obtained due to the following lemma.

**Lemma 1** (J. F. Henriques [35]): If  $X$  is a circulant matrix, the solution (5) can be converted into frequency domain:

$$\mathcal{F}(\mathbf{w}) = \frac{\mathcal{F}^*(\mathbf{x}) \odot \mathcal{F}(\mathbf{y})}{\mathcal{F}^*(\mathbf{x}) \odot \mathcal{F}(\mathbf{x}) + \lambda} \quad (6)$$

where  $\mathcal{F}(\cdot)$  is the Discretized Fourier Transform (DFT) and the superscript  $*$  is the complex conjugate,  $\odot$  and  $\oslash$  are element-wise multiplication and division respectively.

Except for the Fourier transform, all the operations in (6) are element-wise. Therefore, its complexity is dominated by the Fast Fourier Transform (FFT)  $\mathcal{O}(n \log(n))$  where  $n$  is the number of points in the axonometric image. The original solution (5) is dominated by the matrix inversion, whose complexity has a lower and upper bounds, given by matrix multiplication  $\mathcal{O}(n^2 \log(n))$  [36] and Gauss-Jordan elimination method  $\mathcal{O}(n^3)$ . For a  $480 \times 360$  image where  $n = 172800$ , the complexity ratio  $r \in [\mathcal{O}(n^2 \log(n)) / \mathcal{O}(n \log(n)), \mathcal{O}(n^3) / \mathcal{O}(n \log(n))] = [172800, 2480000000]$ , which implies that lots of running time can be saved if the problem (4) is solved by (6).

2) *Non-linear Case*: Data samples may be linearly separable in a high dimension space although they are not in their original space. Suppose  $\phi(\cdot)$  is a high dimension feature space, such that  $\phi: \mathbb{R}^n \rightarrow \mathbb{R}^d$  and  $d \gg n$ . A kernel  $k$  is defined as the inner product of the feature mapping  $\phi$ .

$$k(\mathbf{x}, \mathbf{z}) = \phi(\mathbf{x})^T \phi(\mathbf{z}), \quad (7)$$

where  $\mathbf{z}$  is a test sample. The solution of  $\mathbf{w} \in \mathbb{R}^d$  is expressed as a linear combination of the training data  $\mathbf{x}_i$  in high dimension feature space  $\phi$ :

$$\mathbf{w} = \sum_{i=0}^{n-1} \alpha_i \phi(\mathbf{x}_i). \quad (8)$$

The regression function becomes

$$f(\mathbf{z}) = \mathbf{w}^T \phi(\mathbf{z}) = \sum_{i=0}^{n-1} \alpha_i k(\mathbf{x}_i, \mathbf{z}). \quad (9)$$

Then minimizing the original objective function (4) is equivalent to finding the combination coefficient  $\alpha = [\alpha_0, \alpha_1, \dots, \alpha_{n-1}]^T$ . For the training data  $X$ , the solution of (4) is given by [34].

$$\alpha = (K + \lambda I)^{-1} \mathbf{y}, \quad (10)$$

where  $K$  is the kernel matrix with each element  $k_{ij} = k(\mathbf{x}_i, \mathbf{x}_j)$ . The dimension of  $\alpha$  depends on the number of samples that is the length of  $\mathbf{x}$ . Fortunately, the kernel matrix  $K$  is circulant when  $k(\mathbf{x}_i, \mathbf{x}_j)$  is a Gaussian kernel [35]:

$$k(\mathbf{x}_i, \mathbf{x}_j) = -\frac{1}{2\pi\sigma^2} e^{-\frac{\|\mathbf{x}_i - \mathbf{x}_j\|^2}{2\sigma^2}}. \quad (11)$$

Then (10) can be calculated in frequency domain by time complexity  $\mathcal{O}(n \log(n))$ :

$$\mathcal{F}(\alpha) = \frac{\mathcal{F}(\mathbf{y})}{\mathcal{F}(\mathbf{k}^{\mathbf{xx}}) + \lambda} \quad (12)$$

where  $\mathbf{k}^{\mathbf{xx}}$  is the first row of the kernel matrix  $K = C(\mathbf{k}^{\mathbf{xx}})$ .

When a test sample  $\mathbf{z}$  is given, we want to find its most similar training sample  $\mathbf{x}_i$ . It is very difficult to find explicit  $\phi(\mathbf{z})$  to calculate  $f(\mathbf{z})$ , especially when  $\phi(\mathbf{z})$  has infinite dimensions. An alternative way is to compute the linear combination of kernel functions  $f(\mathbf{z}) = \sum_{i=0}^{n-1} \alpha_i k(\mathbf{z}, \mathbf{x}_i)$  called kernel trick. To guarantee the robustness, we need to test candidates that include all the circular shifts of sample  $\mathbf{z}$ . Define the kernel matrix  $K^{\mathbf{zx}}$  where each element  $K_{ij} = k(\mathbf{z}_i, \mathbf{x}_j)$  and  $\mathbf{z}_i$  is the  $i_{th}$  row of the circulant matrix  $C(\mathbf{z})$ . Suppose that  $\mathbf{f}(\mathbf{z}) = [f(\mathbf{z}_0), f(\mathbf{z}_1), \dots, f(\mathbf{z}_{n-1})]^T$ , from (9), we have

$$\mathbf{f}(\mathbf{z}) = K^{\mathbf{zx}} \alpha. \quad (13)$$

Since  $K^{\mathbf{zx}}$  is a circulant matrix, again we have  $K^{\mathbf{zx}} = C(\mathbf{k}^{\mathbf{zx}})$  where  $\mathbf{k}^{\mathbf{zx}}$  is the first row of  $K^{\mathbf{zx}}$ . From Lemma 1, we can find the response in frequency domain

$$\mathcal{F}(\mathbf{f}(\mathbf{z})) = \mathcal{F}(\mathbf{k}^{\mathbf{zx}}) \odot \mathcal{F}(\alpha) \quad (14)$$

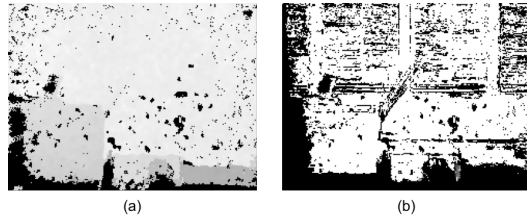


Fig. 6. The left image (a) is an axonometric depth image captured from real time data. The corresponding well-matched points are shown in the right image (b) by pixel intensities. The higher the brightness, the more confidence the matches have.

### C. Image Translation Estimation

The response vector  $\mathbf{f}(\mathbf{z})$  is reshaped back to the original axonometric image plane which is denoted as response matrix  $\mathbf{F}(\mathbf{z})_{N \times M}$ . Since only the zero-shift label  $y_0$  is set as 1, the estimated translation of test sample  $\mathbf{z}$  should be corresponding to the location of the maximum value in the response matrix  $\mathbf{F}(\mathbf{z})$ . Assume the estimated translation of the axonometric image is denoted as  $(\Delta i, \Delta j)$  whose unit is pixel. Then the estimated translation  $(\Delta x, \Delta y)$  in the image plane can be denoted as element-wise multiplication:

$$(\Delta x, \Delta y) = (r_x, r_y) \odot (\Delta i, \Delta j) \quad (15)$$

where  $r_x$  and  $r_y$  are the resolutions of  $x$  and  $y$  directions in the axonometric plane respectively.

As the camera moves, the overlap between the key and new point clouds decreases, resulting in a weak peak strength. A measurement of peak strength (16) is called the Peak to Sidelobe Ratio (PSR). The correlation output  $\mathbf{F}_{i,j}$  is split into the peak which is the maximum value and the sidelobe which is the rest of pixels excluding the peak.

$$PSR = \frac{\max \mathbf{F}_{i,j}(\mathbf{z}) - \mu_s}{\sigma_s} \quad (16)$$

where  $\mu_s$  and  $\sigma_s$  are the mean and standard deviation of the sidelobe. PSR is a similarity measurement of two point clouds and is considered as a trigger to insert a new key point cloud into map. The condition is

$$PSR < T_r \quad (17)$$

where  $T_r$  is a predefined threshold. PSR criterion (17) is not only able to control the minimum confidence of each matching, but also save computational time, especially when the camera is kept still or moving slowly since there is no new training data required.

### D. Depth Translation Estimation

The translation  $\Delta z$  in depth direction is estimated in (18) by the average differences of the matched depth pixels  $I_{i,j}^d$ . To be robust, only those well-matched points are used ( $T_c$  is predefined). Fig. 6 demonstrates an axonometric depth image and its corresponding well-matched points.

$$\Delta z = \text{ave} (s_{\Delta i, \Delta j} (I_{i,j}^d) - I_{i,j}^{kd}) \quad (18)$$

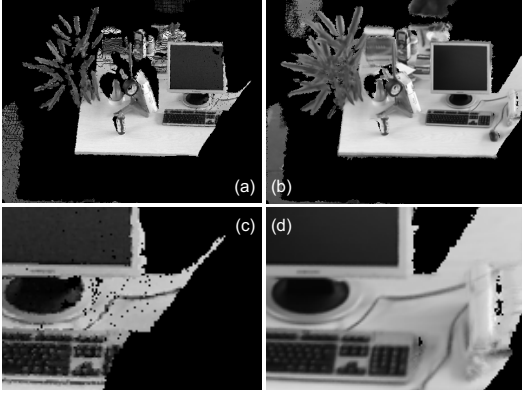


Fig. 7. (a) is a new key cloud. (b) is the refined key cloud during run time. Tests show that the “black holes” in the original axonometric image can be filled by subsequent matched images based on Equation (19). (c) and (d) are the same part of new and refined key point cloud in (a) and (b) respectively. Note that the keyboard on the desk is nearly perfectly complemented. The moving average operation will not make it blurred, if the image translation is estimated correctly.

where  $(i, j) \in \{(i, j) | \rho(s_{\Delta i, \Delta j}(I_{i,j}^c) - I_{i,j}^{kc}) < T_c\}$  and  $\rho(\cdot)$  is a general objective function ( $L_1$ -norm in our tests).  $(\Delta i, \Delta j)$  is the estimated image translation in (15) and  $s_{\Delta i, \Delta j}(\cdot)$  is the shift of an image by  $(\Delta i, \Delta j)$  pixels. The superscript  $d, kd, c, kc$  of image  $I$  are the depth, key depth, color and key color images respectively.

The advantage of (18) is that it only requires the average differences of depth which is extremely fast to be computed and all the well-matched points are able to contribute to the estimation, making it robust to depth noises. Now, we are able to get the translation estimation  $\Delta p = [\Delta x, \Delta y, \Delta z]^T$  based on the decoupled translation in the axonometric plane and depth direction. Next, a refinement of key point clouds will be presented.

### E. Refinement of Key Point Clouds

When the camera is kept still or moving slowly, the overlap between the new and key point cloud is large enough and (17) is not satisfied. The  $k_{th}$  new point cloud  $I_k^{new}$  can be used to refine the key point cloud  $I^{key}$ . A moving average (19) is applied to refine both the color and depth information.

$$I^{key} = \frac{W_{k-1}^{key} \odot I^{key} + s_{\Delta i, \Delta j}^k(W_k^{new} \odot I_k^{new})}{W_{k-1}^{key} + s_{\Delta i, \Delta j}^k(W_k^{new}) + e} \quad (19a)$$

$$W_k^{key} = W_{k-1}^{key} + W_k^{new} \quad (19b)$$

where  $e$  is an infinitesimal term (we set  $1e^{-7}$ ) to prevent division by 0. The weight matrix  $W$  has the same size of the image  $I$  where each pixel presents the weight of that pixel to be fused.  $W_k^{new}(i, j) = \{0, 1\}$  where 1 or 0 indicates whether the pixel  $(i, j)$  can be seen in the original point cloud or not. Thus the matrix  $W_k^{new}$  can be obtained in parallel with the procedure of reprojection.  $W_0^{key}$  is initialized as  $W^{new}$  when the point cloud  $I^{new}$  is inserted as the key frame  $I^{key}$ . Fig. 7 shows an example of new key point cloud and its refined key point cloud by subsequent images. For

axonometric depth image, the only difference is that the term  $I_k^{new}$  in (19a) will be replaced by  $I_k^{new} - \Delta z_k$ , where  $\Delta z_k$  is the estimated translation in the depth direction at time step  $k$ .

## V. EVALUATION

We evaluate our algorithm and compare it with the state of the art methods Volumetric Fusion [37] and RGB-D SLAM [32], [38] in terms of **computational speed**, **map resolution** and **accuracy of estimated trajectory**. All the three indexes are evaluated on the widely used RGB-D benchmark [39] that provides synchronized ground truth from a motion capture system which is also used to produce AHRS data.

We evaluate multi-runs over 10 different datasets each of which contains normal translational and rotational movements by a hand-hold camera. Besides, the datasets fr3/nst and fr3/stf, fr3/stn contain nonstructural/structural environment at near/far viewpoint; fr3/sitting-static and fr3/sitting-xyz contain dynamic objects in the field of view.

Experiments show that hardware platform will have a significant impact on the performance. Hence, we compare the platforms together with the corresponding update rate and map resolution in Table I (NI-SLAM for Evaluation). Typically, higher resolution will result in slower update rate. However, we still achieve the fastest update rate with the highest map resolution using the lowest-power CPU without any GPU devices.

More details about the distribution of update frequency over all the 10 datasets can be found in the boxplot of Figure 8 which shows that all the median update frequencies are above 50Hz. The corresponding statistic performance of the accuracy is shown in Table II. We use the absolute trajectory (ATE) root-mean-square error metric (RMSE) to evaluate our system. The comparison with the state of the art algorithms can be found in Table III where ‘-’ indicates that the data can not be found or that algorithm is not able to produce an estimate on the dataset. The performances of [32], [37], [38] are cited from their papers. Table I and III indicate that we achieve the fastest running speed with the highest map resolution and comparable accuracy.

## VI. ON-THE-FLY TESTING

A very light and challenging hardware platform is chosen to evaluate the performance on low-power system, including a coin size inertial sensor myAHRS+ and the Intel RealSense Robotics Development Kit that features a RealSense R200 Camera and a credit card size board whose details are shown in Table I (NI-SLAM for MUAV). The integrated hardware system is presented in Fig. 1 (c) running with Ubuntu 16.04. We will also release the source codes based on Robot Operating System (ROS) Kinetic Kame.

A work place map created in real-time is shown in Fig. 1 (a) without any post-processing procedure. The map is updated in 15Hz with resolution 0.005m, hence much detail about the environments can be preserved. We also run the proposed framework 5 times in a room with motion capture system. Fig. 9 shows the estimated trajectory from top of

TABLE I

THE HARDWARE USED IN [32], [37], [38]. THE ROUGHLY UPDATE RATES WITH RESPECT TO THE MAP RESOLUTION ARE SHOWN IN THE LAST COLUMN.

Methods	CPU	RAM	GPU	Update Rate/Map Resolution
NI-SLAM for MUAV	Atom x5-Z8350 1.44GHz	2Gb	None	14Hz/0.005m
NI-SLAM for Evaluation	i7-5550U 2.0GHz Dual Core	8Gb	None	50Hz/0.005m
Volumetric Fusion [37]	i7-3960X 3.3GHz Hexa Core	16Gb	nVidia GeForce GTX680	30Hz/0.010m
RGB-D SLAM [32], [38]	i7-***** 3.4GHz Quad Core	8Gb	nVidia GeForce GTX570	30Hz/0.100m

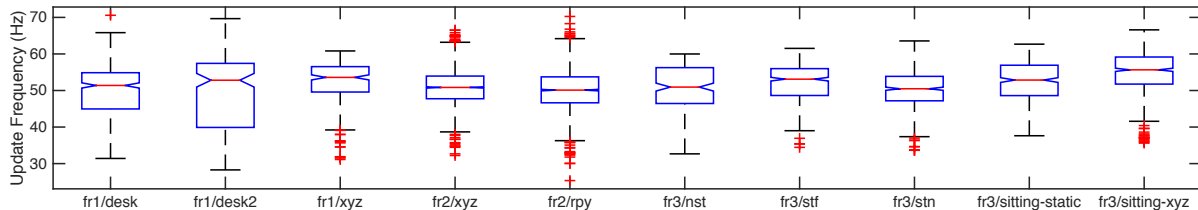


Fig. 8. Update rates are all above 50Hz with the axonometric image size  $360 \times 480$ . The training time of keyframes is also considered in each update.

TABLE II

STATISTIC PERFORMANCE OF ATE ON EVALUATED DATASETS. THE MEAN TRANSLATIONAL AND ANGULAR VELOCITY ARE GIVEN IN  $\bar{v}$  AND  $\bar{\omega}$  RESPECTIVELY. ‘DYNAMIC’ MEANS DYNAMIC OBJECTS CAN BE SEEN IN THE FIELD OF VIEW.

Dataset	RMSE (m)	Mean (m)	Median (m)	Std. (m)	Map Resolution (m)	$\bar{v}$ (m/s)	$\bar{\omega}$ ( $^{\circ}$ /s)	Dynamic
fr1/desk	0.0252	0.0236	0.0216	0.0087	0.0020	0.413	23.32	No
fr1/desk2	0.0598	0.0563	0.0530	0.0200	0.0025	0.426	29.31	No
fr1/xyz	0.0112	0.0097	0.0083	0.0055	0.0035	0.244	8.92	No
fr2/xyz	0.0121	0.0108	0.0102	0.0054	0.0030	0.058	1.72	No
fr2/rpy	0.0269	0.0225	0.0202	0.0147	0.0050	0.014	5.77	No
fr3/nst	0.0171	0.0157	0.0153	0.0068	0.0060	0.299	2.89	No
fr3/stf	0.0137	0.0127	0.0122	0.0051	0.0060	0.193	4.32	No
fr3/stn	0.0193	0.0183	0.0174	0.0061	0.0040	0.141	7.68	No
fr3/siting-static	0.0097	0.0086	0.0077	0.0045	0.0060	0.011	1.70	Yes
fr3/siting-xyz	0.0514	0.0439	0.0382	0.0267	0.0060	0.132	3.56	Yes

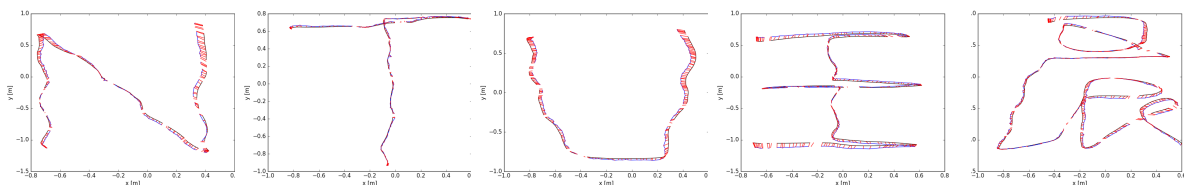


Fig. 9. The differences (red) between the estimated trajectory (blue) and the groundtruth (black) from top of view.

view compared with the groundtruth. Their corresponding update rates and accuracy performance are shown in Fig. 10 and Table IV. It can be seen that, although limited by the low quality point clouds (RealSense Camera produces more noises than Kinect), our proposed framework can still work very well on the ultra-low power system in single thread.

## VII. CONCLUSION

A novel non-iterative inertial-visual framework is proposed in this paper. First, different from existing methods, our algorithm fuses attitude information from AHRS directly and decouples the original 6 DoF data by axonometric projection. Second, by leveraging the property of circulant matrix and also Fourier Transform, we find a non-iterative solution for visual data association, which significantly decreases the computational burden and makes real-time Visual SLAM feasible for MUAV. Last, a fast map refinement/fusion

TABLE III

COMPARISON OF ATE RMSE ON EVALUATED DATASETS. (UNIT: m)

Dataset	NI-SLAM	Vol.-Fusion [37]	RGB-D [32], [38]
fr1/desk	<b>0.025</b>	0.037	0.026
fr1/desk2	<b>0.060</b>	0.071	0.102
fr1/xyz	<b>0.011</b>	0.017	<b>0.021</b>
fr2/xyz	0.012	0.029	<b>0.008</b>
fr2/rpy	<b>0.027</b>	-	-
fr3/nst	<b>0.017</b>	0.031	0.018
fr3/stf	<b>0.014</b>	-	-
fr3/stn	<b>0.019</b>	-	-
fr3/sitting-static	<b>0.010</b>	-	-
fr3/sitting-xyz	<b>0.051</b>	-	-

method is designed based on moving average on rectified point clouds by the estimated translation. To the best of our knowledge, our method is the first non-iterative solution for visual SLAM and is able to achieve the fastest speed with the

TABLE IV

PERFORMANCE OF ATE RMSE ON ‘NI-SLAM FOR MUAV’. (UNIT: m)

Tests	RMSE	Mean	Median	Std.	Resolution
First	0.0318	0.0280	0.0268	0.0148	0.005
Second	0.0140	0.0129	0.0128	0.0054	0.005
Third	0.0327	0.0307	0.0292	0.0111	0.005
Forth	0.0385	0.0345	0.0301	0.0171	0.005
Fifth	0.0313	0.0282	0.0275	0.0135	0.005

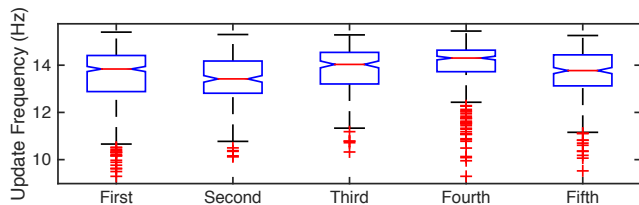


Fig. 10. Update rates on the platform ‘NI-SLAM for MUAV’. The training time of key frames is also considered in each update.

highest map resolution and comparable accuracy compared with the state of the art algorithms.

#### ACKNOWLEDGMENT

The authors would like to thank the help from Mr. Hoang Minh Chung, Mr. Junjun Wang, Dr. Chun-lin Chen, Mr. Tete Ji, Dr. Jinming Xu, Dr. Le Zhang and Dr. Han Zou.

#### REFERENCES

- [1] T. Bailey and H. Durrant-Whyte, “Simultaneous Localization and Mapping (SLAM): Part II,” *Robotics & Automation Magazine*, vol. 13, no. 3, pp. 108–117, 2006.
- [2] P. Henry, M. Krainin, E. Herbst, X. Ren, and D. Fox, “RGB-D Mapping: Using Kinect-Style Depth Cameras for Dense 3D Modeling of Indoor Environments,” *Journal of Robotics Research*, vol. 31, no. 5, pp. 647–663, Apr. 2012.
- [3] J. Fuentes-Pacheco and J. Ruiz-Ascencio, “Visual simultaneous localization and mapping: a survey,” *Artificial Intelligence ...*, 2015.
- [4] D. G. Lowe, “Distinctive Image Features from Scale-Invariant Keypoints,” *International Journal of Computer Vision*, vol. 60, no. 2, pp. 91–110, 2004.
- [5] H. Bay, T. Tuytelaars, and L. Van Gool, “SURF: Speeded Up Robust Features,” in *Computer Vision – ECCV 2008*. Berlin, Heidelberg: Springer Berlin Heidelberg, 2006, pp. 404–417.
- [6] E. Rublee, V. Rabaud, K. Konolige, and G. Bradski, “ORB: An efficient alternative to SIFT or SURF,” in *IEEE International Conference on Computer Vision*. IEEE, 2011, pp. 2564–2571.
- [7] R. Raguram, J.-M. Frahm, and M. Pollefeys, “A Comparative Analysis of RANSAC Techniques Leading to Adaptive Real-Time Random Sample Consensus,” in *Computer Vision – ECCV 2008*. Berlin, Heidelberg: Springer Berlin Heidelberg, 2008, pp. 500–513.
- [8] G. Klein and D. M. Murray, “Parallel Tracking and Mapping for Small AR Workspaces,” in *2007 6th IEEE International Symposium on Mixed and Augmented Reality (ISMAR)*. IEEE, 2007, pp. 1–10.
- [9] C. Forster, M. Pizzoli, and D. Scaramuzza, “SVO: Fast Semi-Direct Monocular Visual Odometry,” *IEEE International Conference on Robotics and Automation*, pp. 15–22, 2014.
- [10] P. J. Besl and N. D. McKay, “A Method for Registration of 3-D Shapes,” *IEEE Transactions on Pattern Analysis and Machine Intelligence*, vol. 14, pp. 1–18, Feb. 1992.
- [11] C. Kerl, J. Sturm, and D. Cremers, “Dense visual SLAM for RGB-D cameras,” in *IEEE/RSJ International Conference on Intelligent Robots and Systems*. IEEE, 2013, pp. 2100–2106.
- [12] D. Gutierrez-Gomez, W. Mayol-Cuevas, and J. J. Guerrero, “Dense RGB-D Visual Odometry Using Inverse Depth,” *Robotics and Autonomous Systems*, vol. 75, pp. 571–583, 2016.
- [13] J. Engel, T. Schöps, and D. Cremers, “LSD-SLAM: Large-Scale Direct Monocular SLAM,” in *Computer Vision – ECCV 2008*. Cham: Springer International Publishing, 2014, pp. 834–849.
- [14] R. A. Newcombe, S. J. Lovegrove, and A. J. Davison, “DTAM: Dense tracking and mapping in real-time,” in *IEEE International Conference on Computer Vision*. IEEE, 2011, pp. 2320–2327.
- [15] S. Omari, M. Bloesch, P. Gohl, and R. Siegwart, “Dense Visual-Inertial Navigation System for Mobile Robots,” in *IEEE International Conference on Robotics and Automation*. IEEE, 2015, pp. 2634–2640.
- [16] F. Fraundorfer and D. Scaramuzza, “Visual Odometry: Part II: Matching, Robustness, Optimization, and Applications,” *Robotics & Automation Magazine*, vol. 19, no. 2, pp. 78–90, May 2012.
- [17] R. Mur-Artal, J. M. M. Montiel, and J. D. Tardos, “ORB-SLAM: A Versatile and Accurate Monocular SLAM System,” *IEEE Transactions on Robotics*, vol. 31, no. 5, pp. 1147–1163, 2015.
- [18] S. Khan and D. Wollherr, “iBUILD: Incremental bag of Binary words for appearance based loop closure detection,” in *IEEE International Conference on Robotics and Automation*. IEEE, 2015, pp. 5441–5447.
- [19] T. Cieslewski, E. Stumm, A. Gawel, M. Bosse, S. Lynen, and R. Siegwart, “Point cloud descriptors for place recognition using sparse visual information,” in *IEEE International Conference on Robotics and Automation*. IEEE, 2016, pp. 4830–4836.
- [20] E. Rosten and T. Drummond, “Machine Learning for High-Speed Corner Detection,” in *Computer Vision – ECCV 2006*. Berlin, Heidelberg: Springer Berlin Heidelberg, May 2006, pp. 430–443.
- [21] J. Engel, J. Stuckler, and D. Cremers, “Large-Scale Direct SLAM with Stereo Cameras,” in *IEEE/RSJ International Conference on Intelligent Robots and Systems*. IEEE, 2015, pp. 1935–1942.
- [22] J. Engel, J. Sturm, and D. Cremers, “Semi-dense Visual Odometry for a Monocular Camera,” in *IEEE International Conference on Computer Vision*. IEEE, 2013, pp. 1449–1456.
- [23] A. Concha, G. Loianno, V. Kumar, and J. Civera, “Visual-inertial direct SLAM,” in *IEEE International Conference on Robotics and Automation*. IEEE, 2016, pp. 1331–1338.
- [24] S. Leutenegger, S. Lynen, M. Bosse, R. Siegwart, and P. Furgale, “Keyframe-Based Visual-Inertial Odometry Using Nonlinear Optimization,” *Journal of Robotics Research*, vol. 34, no. 3, pp. 314–334, Feb. 2015.
- [25] C. Forster, L. Carlone, F. Dellaert, and D. Scaramuzza, “IMU Preintegration on Manifold for Efficient Visual-Inertial Maximum-a-Posteriori Estimation,” in *Robotics: Science and Systems*. Robotics: Science and Systems Foundation, Jul. 2015.
- [26] M. Li and A. I. Mourikis, “High-Precision, Consistent EKF-Based Visual-Inertial Odometry,” *Journal of Robotics Research*, vol. 32, no. 6, pp. 690–711, 2013.
- [27] L. Ma, J. M. Falquez, S. McGuire, and G. Sibley, “Large scale dense visual inertial slam,” *Field and Service Robotics*, 2016.
- [28] N. Engelhard, F. Endres, and J. Hess, “Real-time 3D visual SLAM with a hand-held RGB-D camera,” *Proc. of the RGB-D Workshop on 3D Perception in Robotics at the European Robotics Forum, Vasteras, Sweden*, vol. 180, 2011.
- [29] Y. Ji, A. Yamashita, and H. Asama, “RGB-D SLAM Using Vanishing Point and Door Plate Information in Corridor Environment,” *Intelligent Service Robotics*, vol. 8, no. 2, pp. 105–114, 2015.
- [30] M. Leccadito, T. M. Bakker, R. Niu, and R. H. Klenke, “A Kalman Filter Based Attitude Heading Reference System Using a Low Cost Inertial Measurement Unit,” in *AIAA Guidance, Navigation, and Control Conference*. Reston, Virginia: American Institute of Aeronautics and Astronautics, Jan. 2015.
- [31] S. O. H. Madgwick, A. J. L. Harrison, and R. Vaidyanathan, “Estimation of IMU and MARG orientation using a gradient descent algorithm,” in *2011 IEEE 12th International Conference on Rehabilitation Robotics: Reaching Users & the Community (ICORR 2011)*. IEEE, 2011, pp. 1–7.
- [32] F. Endres, J. Hess, N. Engelhard, J. Sturm, D. Cremers, and W. Burgard, “An Evaluation of the RGB-D SLAM System,” *IEEE International Conference on Robotics and Automation*, pp. 1691–1696, 2012.
- [33] R. M. Gray, “Toeplitz and Circulant Matrices: A Review,” *Foundations and Trends® in Communications and Information Theory*, vol. 2, no. 3, pp. 155–239, 2005.
- [34] R. Rifkin, G. Yeo, and T. Poggio, “Regularized Least-Squares Classification,” *Nato Science Series Sub Series III Computer and Systems Sciences*, vol. 190, pp. 131–154, 2003.
- [35] J. F. Henriques, R. Caseiro, and P. Martins, “High-Speed Tracking

- with Kernelized Correlation Filters,” *IEEE Transactions on Pattern Analysis and Machine Intelligence*, vol. 37, no. 3, pp. 583–596, 2015.
- [36] R. Raz, “On the Complexity of Matrix Product,” *Siam Journal on Computing*, vol. 32, no. 5, pp. 1356–1369, 2003.
- [37] T. Whelan, M. Kaess, H. Johannsson, M. Fallon, J. J. Leonard, and J. McDonald, “Real-Time Large-Scale Dense RGB-D SLAM with Volumetric Fusion,” *Journal of Robotics Research*, vol. 34, no. 4-5, pp. 598–626, 2015.
- [38] F. Endres, J. Hess, J. Sturm, D. Cremers, and W. Burgard, “3-D Mapping With an RGB-D Camera,” *IEEE Transactions on Robotics*, vol. 30, no. 1, pp. 177–187, 2014.
- [39] J. Sturm, N. Engelhard, F. Endres, W. Burgard, and D. Cremers, “A benchmark for the evaluation of RGB-D SLAM systems,” in *IEEE/RSJ International Conference on Intelligent Robots and Systems*. IEEE, 2012, pp. 573–580.